An Angle-Resolved Photoemission Spectroscopy Study of $Tl_2Ba_2CuO_{6+\delta}$

Analysis of recent results and the construction of a new system

by

Jeffrey Daniel Frederick Mottershead

B.Sc., The University of Alberta, 2001

A THESIS SUBMITTED IN PARTIAL FULFILMENT OF
THE REQUIREMENTS FOR THE DEGREE OF

MASTER OF SCIENCE

in

The Faculty of Graduate Studies

(Physics)

THE UNIVERSITY OF BRITISH COLUMBIA

April 22, 2005

Abstract

Recent angle-resolved photoemission spectroscopy (ARPES) results on the high-temperature superconductor (HTSC) $Tl_2Ba_2CuO_{4+\delta}$ (Tl2201) are presented. A very overdoped sample with a T_c of 30 K was found to have a Fermi surface consisting of a large hole pocket centered at (π, π), which is approaching a topological transition. A superconducting gap consistent with a $d_{x^2-y^2}$ order parameter was detected. In contrast with the underdoped HTSCs, where the quasiparticle (QP) linewidth at the top of the band is maximal in the antinodal direction and minimal in the nodal direction, overdoped Tl2201 was revealed to have a reverse nodal/antinodal anisotropy, with sharp QP peaks in the antinodal region and broader peaks in the antinodal region.

The Tl2201 results establish Tl2201 as a valuable material for exploring the overdoped side of the phase diagram with ARPES. They also raise numerous questions that demand further ARPES measurements over a broader range of dopings, as well as temperature-dependent measurements.

In parallel with the Tl2201 research, a new in-house ARPES system is being constructed at University of British Columbia (UBC). The ARPES system under construction at UBC incorporates a molecular beam epitaxy (MBE) system for the growth of a much broader range of materials than can typically be studied by ARPES. Novel design techniques to improve the accuracy of ARPES measurements are presented.

Contents

List of Figures

Acknowledgements

I am extremely grateful to my supervisor, Dr. Andrea Damascelli, for focusing my efforts in the right directions, regardless of the level of resistance I offered, and for valuable lessons on my psychology [1, 2]. Thanks also to Dr. Nik Ingle, who taught me how to do ARPES in the first place. I am also grateful to Dr. Ruixing Liang and Darren Peets, who grew the $Tl_2Ba_2CuO_{4+\delta}$ crystals which made this work possible. Mauro Platé was instrumental in the data analysis in this work. Much of the work on the new chamber has been done by undergraduate students Fei Cio, Shannon Wang, Paul Bloudoff, Robin Norman, James Charbonneau and Tor Pedersen. While the work of all of these students has been extremely valuable, special accolades go to Tor, who has taken on a role closer to that of a grad student, or even a postdoctoral fellow. Special thanks goes to LaTeX master Scott Webster, who provided invaluable tech support in exchange for me ruining his car. Finally, and most importantly, I need to thank my wife, Iva Cheung, who has (mostly) patiently endured the late nights that were required to get this project more or less done, and who made me write my thesis, then proceeded to help make figures for it and edit the entire thing.

Chapter 1

Introduction

Since high-temperature ceramic superconductors were discovered in 1986 [3], they have attracted attention both for their potential technological uses and because they presented a scientific challenge. The Bardeen-Cooper-Schrieffer (BCS) theory, which satisfactorily explains superconductivity in Fermi-liquid-like metals, does not have the correct starting assumptions to model the high-T_c superconductors (HTSCs). A theory of the HTSCs has been elusive, despite a long-term focused effort, due to the difficulty inherent in modelling the strong electron-electron interactions present in these materials. The presence of these interactions makes the goal of finding a model for the HTSCs part of a larger objective – that being the construction of a model that explains the properties of systems with strong electron-electron interactions. Despite a strong effort for many years, however, there is no agreement on a theoretical model for the HTSCs, partially due to the fact that strong electron-electron interactions present a difficult system to model, and partially because experimental results from different techniques are best suited for measurements on different compounds; thus, forming a coherent picture of the experimental results is difficult. $Tl_2Ba_2CuO_{6+\delta}$ (Tl2201) offers an opportunity to do angle-resolved photoemission spectroscopy (ARPES) studies on a material that has a high T_c, yet does not have many of the electronic and structural complications that other materials suited to ARPES have.

In this work, ARPES results from work done at the Swiss Light Source (SLS) using the Surface and Interface Spectroscopy (SIS) beamline are presented. In parallel with the work done at the SLS, construction of a new in-house ARPES system has begun. The goals of the new ARPES system are two-fold: as well as achieving lower temperatures and higher resolution than the existing state-of-the-art, we also are connecting a molecular beam epitaxy (MBE) system to our ARPES chamber, such that we can do ARPES studies of materials that either cannot be grown as crystals, or do not cleave well enough to be studied by ARPES through conventional means.

1.1 Correlated systems

The physics of simple metals, semiconductors, and many ionic compounds are understood and modelled successfully by calculating the behaviour of free electrons interacting with a periodic potential of atomic nuclei [4]. Theoretical modelling of these materials agrees well with measurements and can be used to predict an impressive array of properties, such as thermal conductivity, AC and DC electrical conductivity, the Hall coefficient and magnetoresistance, to name a few. Elementary calculations of these quantities rest heavily on the free-electron approximation, and corrections due to electron-electron interactions are handled perturbatively [4].

At the other end of the spectrum, we are able to accurately model molecular chemistry in the paradigm of bound electrons [5]. Hybridization of molecular electronic orbitals provides a reliable method for computing electronic states in organic molecules.

Between these two canonical regimes, however, there is a wide range of materials that have electrons that are not bound to specific lattice sites, but do interact heavily with each other. These materials, known as correlated systems, have a staggering range of properties that are unexpected on the basis of the independent particle picture, and these properties can change dramatically with small changes in doping, lattice constants, temperature and pressure, as a result of electron-electron and electron-phonon interactions giving rise to many different competing phases. While these interactions are responsible for the broad range of properties in correlated systems, it is also their presence that makes calculations notoriously difficult. Due to presence of strong correlations, calculations of the properties of these materials are inherently many-body problems, with no standard technique for simplifying the problem. In order to effectively model the electron-electron interactions, an experimental model for the spectral function is needed, making spectroscopic studies of these materials one of the main thrusts of the current experimental effort.

1.2 The cuprates

Among correlated systems, materials with 3d and 4f-orbital valence electrons stand out in particular, because the 3d and 4f electrons from the metals can range from highly correlated to nearly free with small changes in tunable parameters, such as temperature, interatomic spacing or doping. By adjusting

these parameters, dramatic changes in the properties of these materials take place. As well as the potential for technological applications, the transition metal oxides provide much of the motivation behind modern solid state physics, since we should be able to continuously change the Hamiltonian of these materials, corresponding to changes in tunable parameters, and observe the same dramatic changes of the properties in our calculations that we do in experiment. Two-dimensional copper oxides are of special interest, both scientifically and technologically, as they change from being an antiferromagnetic insulator to a HTSC, and finally to a metallic but non-superconductive state, ostensibly a Fermi liquid, as a function of doping.

1.3 Angle-resolved photoemission spectroscopy

While many different types of measurements have made important contributions to our understanding of the HTSCs [6], ARPES gives the most direct measurement of the momentum-resolved electronic structure. Since electron-electron correlation contributes to spectral weight away from the bands predicted from non-interacting electron calculations, ARPES measurements allow for a relatively direct probe of electron-electron correlations. To a first approximation, the copper d-electrons responsible for superconductivity have no dispersion perpendicular to the copper-oxygen plane. Thus, the d-electrons can be thought of as two-dimensional (2D), making them ideal for studies by ARPES, in which the components of electron momentum parallel to the surface are conserved during photoemission, while the component perpendicular to the surface is not [7].

The simplest model of photoemission is as follows: a photon of known energy promotes an electron of a given energy ϵ and momentum k to a state with the same momentum k and an energy $\epsilon + \hbar\omega$. The electron is assumed to immediately exit the surface of the material, thereby losing ϕ, the work function, from its energy, giving the electron a final energy of $\epsilon + \hbar\omega - \phi$. While leaving the material, the momentum parallel to the surface of the sample is conserved, but perpendicular to the sample, there is lack of symmetry, and the momentum perpendicular to the plane is not conserved. The fact that the momentum is not conserved in the perpendicular direction is not a problem in the analysis of 2D electrons, however, where there is no electronic dispersion perpendicular to the surface of the sample. By measuring the photoelectron energy, and the angle of emission, from which the parallel component of momentum is readily

calculable, the electronic dispersion of a 2D material can be readily determined. The electronic structure of the CuO_2 band, thought to be responsible for superconductivity in the cuprates, is sufficiently close to 2D that they are often treated as 2D. As well as having a quasi-2D electronic structure, the cuprates further lend themselves to ARPES studies as they naturally cleave parallel to the copper-oxide planes. Thus, ARPES data yield direct information about the single-particle spectral function for occupied states, and hence is a valuable and unique tool for determining the electronic origins of the exotic properties found in the cuprates. Note that the simple model described above does not take into account scattering or surface effects. For a more complete model of the photoemission process, see Hüfner [7], and for a review of ARPES on the cuprates, see Damascelli et al. [8].

1.4 $Tl_2Ba_2CuO_{6+\delta}$ as a material for ARPES studies

Certain families of cuprates, particularly $Bi_2Sr_2CuO_{6+\delta}$ (Bi2201), its bilayer cousin $Bi_2Sr_2CaCu_2O_{8+\delta}$ (Bi2212) and $La_{2-x}Sr_xCuO_4$ (LSCO) have been extensively studied by ARPES. While these studies have produced many valuable results [8], they have been complicated by material issues. Bi2201 and Bi2212, for instance, cleave very readily, making it easy to get a vacuum-clean surface on which to do photoemission work. Bi2201 and Bi2212 are therefore standard materials for ARPES studies, but from a theoretical modelling perspective, they are not at all ideal. Further, when studying Bi-based cuprates, one is faced with the choice of studying either the single-layer compound Bi2201, which has a low T_c, or Bi2212, which has a much higher T_c, but also has the problem of being a bilayer compound, where there is inter-layer coupling between neighboring copper-oxygen planes, complicating both analysis of the ARPES spectra and the theoretical modelling of the compound. Furthermore, Bi2201 and Bi2212 are not well suited to bulk sensitive measurements, complicating the comparison of cuprate data from complimentary techniques.

The thallium compound $Tl_2Ba_2CuO_{6+\delta}$ (Tl2201) presents a unique opportunity to untangle the physics of high-temperature superconductivity from other material issues. Tl2201 is a single-layer compound with a very high T_c of 93 K at optimal doping [9], and can be grown with a clean crystal structure over a broad doping range. Further, Tl2201 can be grown in the heavily overdoped

side of the phase diagram, where very little ARPES work has been done.

Tl2201 has not been studied by ARPES extensively due to technical difficulties. At the required temperatures for growing Tl2201 crystals, the highly toxic TlO has a significant vapour pressure. Despite the hazards inherent in its growth, Tl2201 has been synthesized, but attempts at ARPES issues have been stymied by material issues. Despite these difficulties, the unique opportunity provided by Tl2201 justifies the effort needed to overcome them. In this thesis, Tl2201 ARPES data taken at the Swiss Light Source on the Surface and Interface Spectroscopy beamline is presented.

1.5 Construction of an in-house ARPES system

Concurrent with the Tl2201 work, the development of a new in-house ARPES system at the University of British Columbia has been undertaken. While developments in electron analyzers have allowed measurements of higher and higher angular and energy resolution, these advances have made the requirements on the surrounding chamber more demanding. In order to capitalize on the increased analyzer resolution, stray electric and magnetic fields in the chamber have to be correspondingly lower, the angular positioning of the sample has to be at least as accurate as the angular resolution of the analyzer, and cryostat temperatures and chamber pressures have to be lower. While each of these design goals by themselves do not present a major challenge, accomplishing them all in the same system provides many unique difficulties. As well as achieving a new level of resolution and a new low for sample temperatures in a movable cryostat, the new system will have a unique advantage of being coupled to a small MBE, which will be used to grow samples and pass them in vacuo to the ARPES system, broadening the scope of ARPES from the narrow set of samples that cleave readily to the very broad range of substances that can be grown by MBE. Furthermore, by growing on substrates of varying lattice constants, the interatomic distance of the material being studied can be adjusted, giving another degree of freedom on top of doping and temperature that can be used to tune the physical properties of the system under study. While this system is not yet completed, results from preliminary testing, as well as some novel design techniques, are presented.

Chapter 2

ARPES on $Tl_2Ba_2CuO_{6+\delta}$

Despite a growing body of ARPES measurements of various families of cuprate superconductors and many intriguing results, there are still profound disagreements as to the meaning of many of these results [8]. Above and beyond the theoretical challenge of modelling correlated electrons, much of the difficulty comes from material issues of various types. Only a few of the known families of cuprates cleave sufficiently cleanly to allow ARPES measurements on crystals, and the synthesis of MBE and ARPES has yet to generate new results. Of the families that have been studied by ARPES, there are family-specific problems.

The bulk of ARPES studies to date have focused on $Bi_2Sr_2CuO_{6+\delta}$ (Bi2201), $Bi_2Sr_2CaCu_2O_{8+\delta}$ (Bi2212) and $La_{2-x}Sr_xCuO_4$ (LSCO). Each of these materials has provided valuable results, but in each family, complexities unrelated to superconductivity are present in the band structure, and the fact that these materials grow non-stoichiometrically have obscured a theoretical interpretation [8, 10].

Producing high-quality cleaved surfaces in LSCO is difficult, making ARPES studies challenging, and the presence of lattice distortions and spin/charge instabilities create complications in the electronic structure of the material, which are difficult to divorce from the signatures of superconductivity [8]. Further, LSCO is difficult to grow without introducing chemical inhomogeneity. The substitutions have a strong effect on superconductivity, as the site of the substitution is neighbouring the copper-oxygen plane.

In Bi2212, superstructure modulations with a periodicity of 27Å make the unit cell much five times larger than the unit cell would be in the absence of the superstructure modulations, and hence, its corresponding Brillouin zone (BZ) is one fifth the size of a Brillouin zone of a modulation-free crystal. However, researchers focus on the latter, larger Brillouin zones, as the smaller zone's features are too faint to prove useful for analysis. As a result, there exist not only the Fermi surface (FS), but also faint Fermi surface replicas. These are known as the umklapp bands [8]. Further, Bi2212 has shadow bands – Fermi surface repli-

cas shifted by $(\pi/2,\pi/2)$. There are several competing theories on the origin of the shadow bands [8]. Finally, Bi2212 has bilayer band-splitting, which is caused by the electronic structure of the neighbouring copper-oxygen planes splitting into bonding and antibonding bands. The presence of bilayer splitting, umklapp bands and shadow bands often obscures the analysis of ARPES spectra of Bi2212. Further, in many instances, it is difficult to determine whether features observed are genuinely features related to superconductivity or merely consequences of the complications in the structure of Bi2212. Furthermore, Bi2212 grows best at optimal doping, but is difficult to synthesize over a broad doping range, especially in the overdoped regime, making studies of the evolution of properties over the entire phase diagram difficult.

Bi2201 is a single-layer compound, and thus does not exhibit the bilayer splitting present in Bi2212. That said, Bi2201 does not have a high T_c, which likely makes the hallmarks of superconductivity less apparent. The umklapp and shadow bands are still present as in Bi2212, and like Bi2212, it can only be easily grown over a limited doping range. Overdoped Bi2201 is not readily synthesized.

In contrast, $Tl_2Ba_2CuO_{6+\delta}$ (Tl2201) has a number of properties that make it ideal for photoemission studies. Tl2201 is a single-layer compound, so there is no bilayer splitting. Tl2201 can be grown over a broad doping range, and thus presents a unique opportunity to do ARPES measurements on a single compound, from optimally doped to highly overdoped, where there are indications that the normal state is a Fermi liquid [11]. Although understanding the transition from the superconducting state to a metallic state is likely critical for a theory of high-T_c superconductivity, very little ARPES research has been done on this part of the phase diagram, as Bi2212 and LSCO both suffer from harmful cation disorder [10] at higher dopings. Cation disorder is not nearly as problematic in Tl2201, where the disorder is manifested as non-stoichiometric oxygen doping and Cu-Tl substitution, both occurring in the TlO planes, far from the CuO_2 planes, making it an ideal candidate for ARPES studies at higher dopings. The crystal structure is well-ordered, with flat, distantly spaced copper-oxygen planes. This reduced disorder may be the reason why Tl2201 has a T_c of 93 K at optimal doping, which is among the highest of single-layer compounds [10].

Although little ARPES work has been done on Tl2201 until now, significant results have been achieved via other experimental techniques. Neutron diffraction has revealed that the non-stoichiometric oxygen is located between the Tl-O layers [12]. The fact that the non-stoichiometric oxygen is isolated from

the Cu-O planes is likely important to the high T_c of optimally doped Tl2201 [10]. A magnetic resonant mode had been observed by neutron scattering [9]. This magnetic resonant mode has been observed in Bi2212 and $YBa_2Cu_3O_{6+\delta}$ (YBCO) [13], but had not previously been observed in a single-layer compound, and thus, it is unclear whether or not the mode is a unique property of bilayer compounds. A pure d-wave order parameter was demonstrated for optimally and overdoped Tl2201 by tunnelling measurements [14]. Heat transport measurements on overdoped Tl2201 (T_c = 15 K) present compelling evidence that the electrons at this doping level form a Fermi liquid. Further, these measurements put an upper bound on any subdominant order parameter of 0.5%[11], providing further evidence for a pure d-wave order parameter. Angular magnetoresistance oscillation measurements (AMRO) indicate a coherent three-dimensional Fermi surface, which is 2D only at high-symmetry points [15].

Previous ARPES measurements on Tl2201 have been stymied by the short lifetimes of the cleaved surfaces. This work presents the first extensive ARPES measurements of overdoped Tl2201 crystals. These results allow a determination of the Fermi surface and give detailed information about the quasiparticle (QP) dispersion. While the Fermi surface is consistent with calculations and previous measurements, and the superconducting gap is consistent with a d-wave order parameter, unexpected results are observed for the lifetimes of the QP excitations. Previous ARPES measurements on the cuprates have focused on the underdoped and optimally doped regimes, and have observed sharp, well-defined QP peaks at (π/2,π/2), broad peaks at (π,0), and a broadening with increasing binding energy over the entire electronic structure [8, 16, 17]. In contrast, we observe sharp peaks near (π,0) and broad features at (π/2,π/2). Further, while the expected behaviour of the QP linewidth increasing with binding energy is observed at (π/2,π/2), the opposite is seen at (π,0).

The research presented was done at the Swiss Light Source, on the Surface and Interface Spectroscopy beamline, with circularly polarized 59 eV photons. The hemispherical electron analyzer used was the Scienta SES-2002 analyzer, which has an energy resolution of 24 meV and an angular resolution of 0.2°. The samples used were grown using a copper-rich self-flux method and were annealed in controlled oxygen partial pressures to produce overdoped samples with T_c's ranging from 5 to 90 K. The high quality of the samples is demonstrated by the narrow superconducting transition widths of 0.7 and 7 K for samples with T_c's of 67.7 and 24 K, respectively (see Figure 2.1). The full-width half-maximum (FWHM) of the (0 0 10) X-ray rocking curve is 0.034°, indicating a good cyrstal

structure (see Figure 2.2)[18].

Measurements were taken on two overdoped samples with T_c's of 63 and 30 K, henceforth referred to as Tl2201-OD63 and Tl2201-OD30, respectively. The vast majority of the data taken was on Tl2201-OD30, which has sufficient information for a FS map and a study of QP lineshape anisotropy. The Tl2201-OD63 data did not allow a FS mapping, but did provide QP lineshapes in the nodal and antinodal directions. The stoichiometry of the crystals is $Tl_{(1.88)1}Ba_2Cu_{(1.11)2}O_{6+\delta}$ with the departure from ideal stoichiometry corresponding to Cu substitution on the Tl site [12]. The samples were cleaved in situ at 10 K, and were kept at 10 K and in a pressure of 6×10^{-11} mbar for the duration of the experiment.

2.1 Data analysis on Tl2201-OD30

The manipulator at the SIS beamline allows for two angular degrees of freedom. The entire cryostat can be rotated about its axis, which is oriented vertically, and the sample holder can be rotated about an axis normal to face where the sample is mounted. The SIS geometry thus allows data to be taken along momentum directions radially outwards from the normal to the sample holder. For a sample mounted parallel to the sample holder, this would mean data would be taken along cuts radially outwards from Γ. Tl2201-OD30 was mounted off-normal, such that data was taken radially from a point near, although not exactly, (π, π), which allowed many of the sets of spectra taken to cross the FS at approximately normal.

Typical ARPES data obtained from Tl2201-OD30 are shown in Figure 2.3, along with Fermi surfaces derived from our band-structure calculations within the local density approximation (LDA) (a), and a tight-binding fit of the experimentally determined FS (d). Our band-structure calculations agree with previously published work [19].

Data was taken over two irreducible symmetry units in two BZs, allowing the exact sample alignment to be determined by imposing the requirement that one symmetry unit can be downfolded directly onto the other. This requirement uniquely and accurately determines the alignment of the sample [20].

The spectra in Figures 2.3b and 2.3c were measured along directions corresponding to the arrows in Figure 2.3a, crossing the FS near the nodal and antinodal regions, respectively. In Figure 2.3b, near the nodal region, the quasipar-

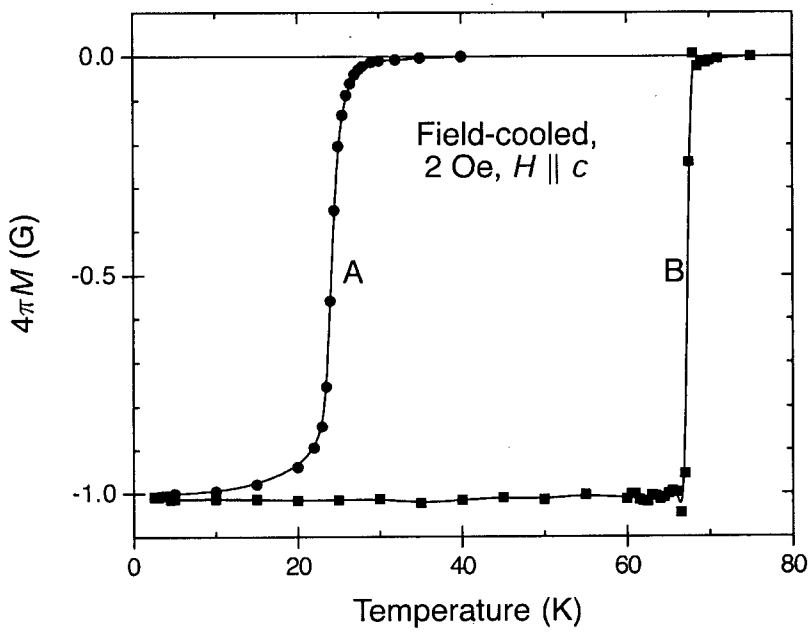

Figure 2.1: Field-cooled magnetization curves for crystals annealed in an O_2 partial pressure of 10^{-6} mbar at 290°C for 14 days (circles) and 10^{-7} mbar at 430°C for 6 days (squares), with T_c's of 24 and 67.7 K, respectively. (Reproduced from Peets et al. [18])

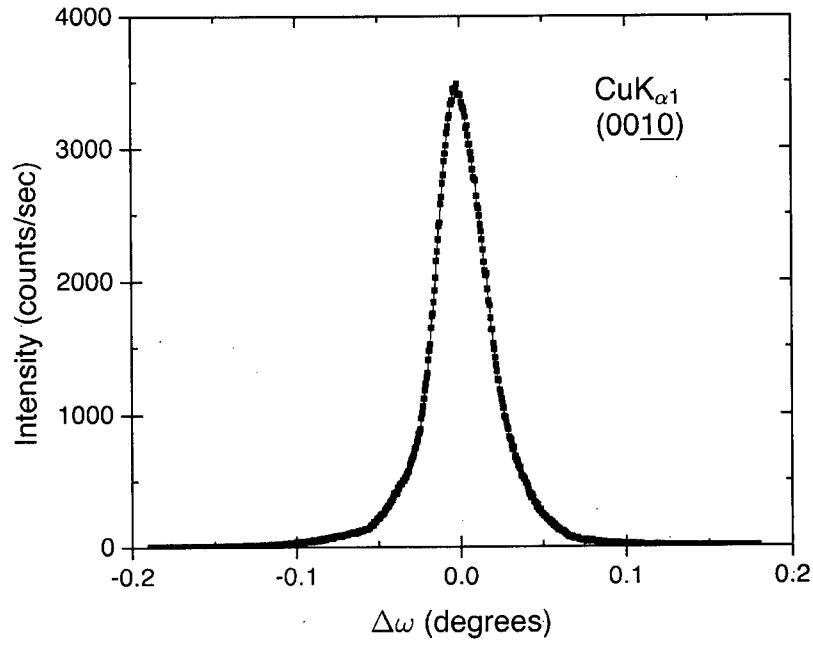

Figure 2.2: (0 0 10) X-ray rocking curve for a typical crystal (T_c = 67.7 K): the FWHM is 0.034°. (Reproduced from Peets et al. [18])

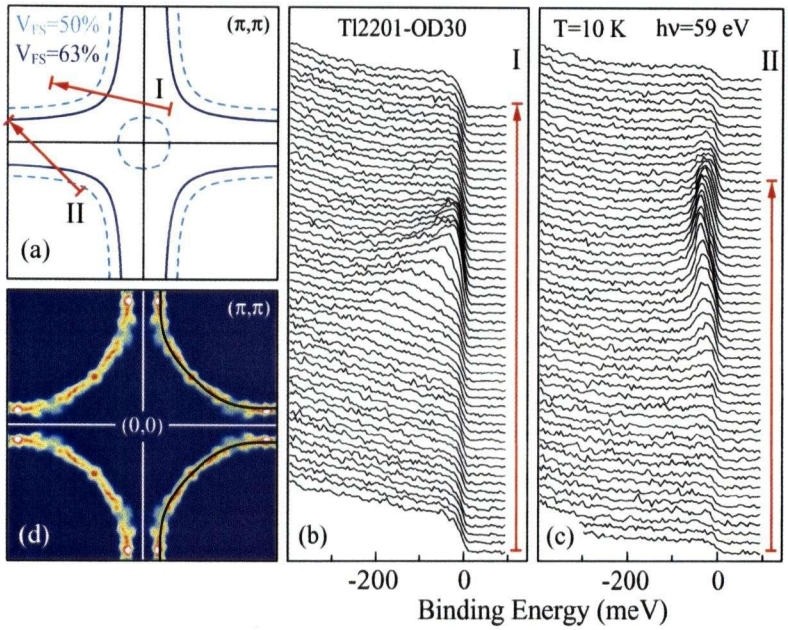

Figure 2.3: LDA Fermi surface for two different doping levels corresponding to a volume of 50% (cyan, dashed) and 60% (blue, solid) of the Brillouin zone. (b,c) ARPES spectra taken at $T = 10$ K on Tl2201-OD30 along the directions marked by the arrows in (a). (d) ARPES FS of Tl2201-OD30 along with a tight-binding fit of the data (black lines).

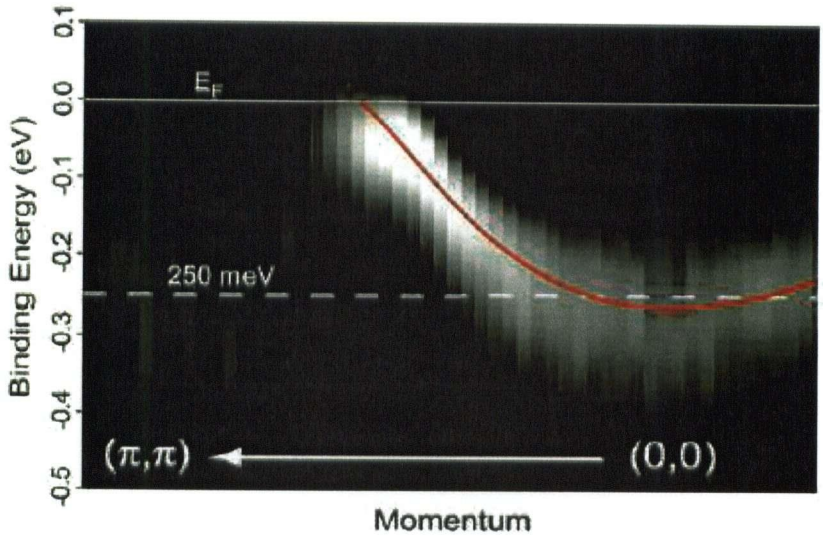

Figure 2.4: Second derivative of the APRES spectra in Figure 2.3b with respect to binding energy.

ticle (QP) peak shows a strong dispersion, which is clearly evident to 150 meV below the Fermi energy (E_F). This dispersion can be seen more clearly by plotting the second derivative of the ARPES spectra with respect to the binding energy. Figure 2.4 shows a result of this analysis for the spectra in Figure 2.3b, showing that the QP peak can be followed to $\sim$ 250 meV binding energy, where the band bottom can be seen. In Figure 2.3c, the band is much shallower, with the van Hove singularity located at $\sim$ 39 meV below E_F.

The ARPES FS is obtained by first normalizing the ARPES spectra at high binding energies and then integrating the ARPES spectra over a $\pm$5 meV window about E_F. This procedure was done over the entire data set, which covers more than one quadrant in two different BZs. The results are then downfolded to the reduced zone scheme. This procedure was used in Damascelli et al. [20] and serves a number of purposes. This procedure serves as a criterion for determining the alignment of the sample. Only if the alignment of the sample is correctly determined will points on the FS from the two different zones be mapped directly on top of each other. The signal-to-noise ratio is also enhanced

by using this technique, as, for each point on the reduced zone, at least two sets contribute to it. Next, the FS is symmetrized with respect to the zone diagonal, $(0,0) - (\pi,\pi)$, averaging over all identical symmetry points. This serves to further increase the signal-to-noise ratio, and to remove any artifacts pertaining to the anisotropy in angular resolution due to the experimental geometry [20]. Note, however, that the resolution anisotropy problems are inherently less severe for our measurement geometry of rotating approximately about (π,π) than for the conventional motion about Γ (see Figure 2.6). It should be noted that at $T = 10$ K, a d-wave superconducting gap is open along the FS. As a result, the procedure described above returns the loci of the minimum gap. Note, though, that these points do correspond to the underlying normal-state FS crossings, as can be seen in Figure 2.5. Calculations of the Bardeen-Cooper-Schrieffer (BCS) spectral function above and below T_c give this result exactly. For the HTSCs, there is no accepted theoretical result, but it is not unreasonable to expect that some aspects of BCS theory will apply to the overdoped side of the phase diagram, where the cuprates are believed to exhibit more conventional behaviour. In fact, the gap structure shown in Figure 2.5 agrees qualitatively with BCS theory, with the minimum gap being at the same location as the Fermi-crossing in the normal state.

The FS found for Tl2201-OD30 is a hole-pocket centered about (π,π). As can be seen by the low binding energy ($\sim$39 meV) of the van Hove singularity in the antinodal direction (see Figure 2.3), the FS appears to be approaching a topological transition from hole-like to electron-like. The volume of the FS is $63 \pm 2\%$ of the BZ, which corresponds to a carrier concentration of 1.26 ± 0.04 holes/Cu atom. This agrees very well with Hall-coefficient [22] and AMRO [15, 23] experiments, which found FS volumes of 1.3 holes/Cu atom on a sample with a T_c of 15 K, and 1.24 holes/Cu atom on a sample with a T_c of 20 K, respectively. All of these measurements indicate that the low-energy electronic structure of highly overdoped Tl2201 is dominated by a single CuO band. In the LDA calculations of Figure 2.3a (cyan, dashed), for undoped Tl2201, we see a small electron pocket coming from the TlO band. Neither ARPES nor AMRO measurements show any evidence for such an electron pocket. This result should be expected, as the samples under study are sufficiently doped that if the chemical potential in the LDA calculations is adjusted in a rigid-band fashion, the TlO band is emptied. Even in the absence of excess oxygen ($\delta = 0$), the holes introduced by the residual non-stoichiometry (Cu^{2+} substituted for Sr^{3+}) are responsible for $\sim$0.14 hole per formula unit, which is sufficient to empty

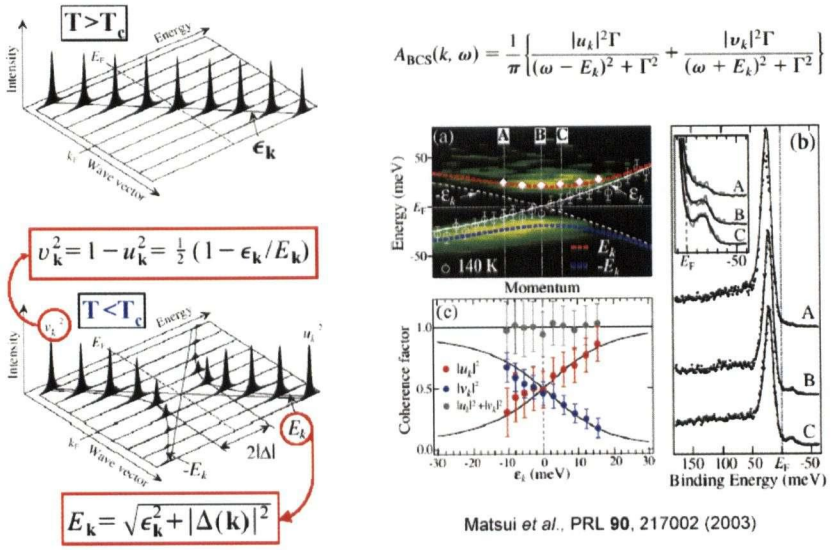

Figure 2.5: (Left) Change in the BCS spectral function across T_c, showing the opening of the gap, the backward dispersion of the Bogoliubov QPs, and their intensity decrease upon approaching k_F due to the presence of coherence factors u_k, v_k. (Right) ARPES results from Bi2223 showing good qualitative agreement. (Reproduced from Matsui et al. [21])

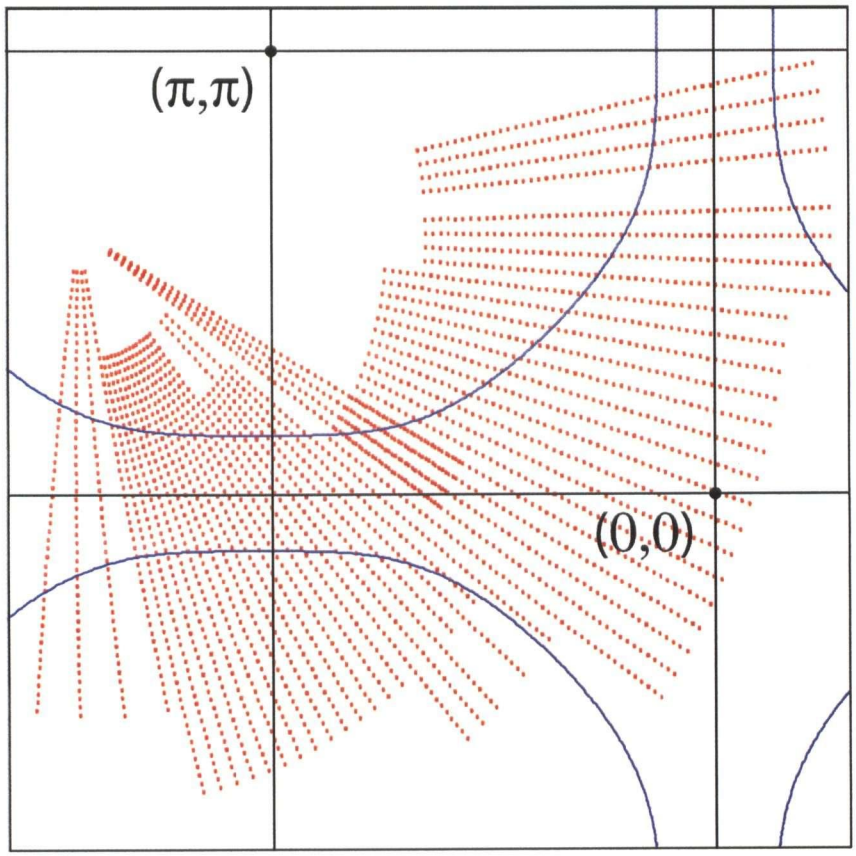

Figure 2.6: Direction of the cuts in momentum space on which ARPES data were obtained for Tl2201-OD30 (red). Momentum space is represented in the repeated zone scheme, with the tight-binding FS included for reference (blue). Data is seen to cover two irreducible symmetry units, and multiple BZs.

the TlO band. In fact, the non-stoichiometry of Tl2201 may push the $\delta = 0$ system sufficiently far from half-filling to explain why it is not a charge transfer insulator like undoped LSCO [23].

The ARPES (Figure 2.3d) and AMRO (Figure 2.7) Fermi surfaces are in good agreement with each other, but they are notably rounder than in the LDA calculations (Figure 2.3a). The LDA calculations could be improved by including correlation effects and the effects of doping beyond a rigid-band approximation. The ARPES data can alternatively be modelled by fitting the parameters in the tight-binding dispersion [13]

$$\epsilon_{\mathbf{k}} = \mu + \frac{t_1}{2}(\cos k_x + \cos k_y) + t_2 \cos k_x \cos k_y + \frac{t_3}{2}(\cos 2k_x + \cos 2k_y) + \\ + \frac{t_4}{2}(\cos 2k_x \cos k_y + \cos k_x \cos 2k_y) + t_5 \cos 2k_x \cos 2k_y.$$

The results of the fit are shown in Figure 2.3d (black lines). The fit not only reproduces the FS, but it also matches the QP energy well at $(0,0)$, and very well at $(\pi,0)$ (see Figures 2.8f, g). Values for the fit parameters are as follows: $\mu = 0.2438$, $t_1 = -0.725$, $t_2 = 0.302$, $t_3 = 0.0159$, $t_4 = -0.0805$, $t_5 = 0.0034$.

Figure 2.8 shows the analysis of ARPES spectra taken in the antinodal region on Tl2201-OD30, demonstrating a superconducting gap consistent with a $d_{x^2-y^2}$ form (i.e., $\cos k_x - \cos k_y$). It is a standard technique to follow the opening of the superconducting gap via a shift in the leading edge midpoint (LEM) as a function of temperature [8]. Unfortunately, it was found that all angle-dependent information in the ARPES spectra was lost if the cyrostat temperature got significantly above 10 K. It is not clear whether this is a result of something extrinsic, like outgassing of the cyrostat, or an intrinsic problem with surface reconstruction of overdoped Tl2201 above 10 K. Regardless of its origin, this effect rendered it impossible for a temperature-dependent study to be done. Nevertheless, a superconducting gap consistent with a d-wave order parameter can be clearly seen in the symmetrization of the nodal and antinodal spectra [24, 25]. While this procedure does not return a quantitative value for the size of the superconducting gap, it provides a qualitiative criterion for determining whether or not there is a Fermi crossing, and hence whether or not a superconducting gap has opened. In the symmetrized spectra, the presence of a peak in the spectra at E_F indicates a crossing. This crossing is clearly seen in the nodal direction (Figure 2.8a), but not in the antinodal direction (Figure

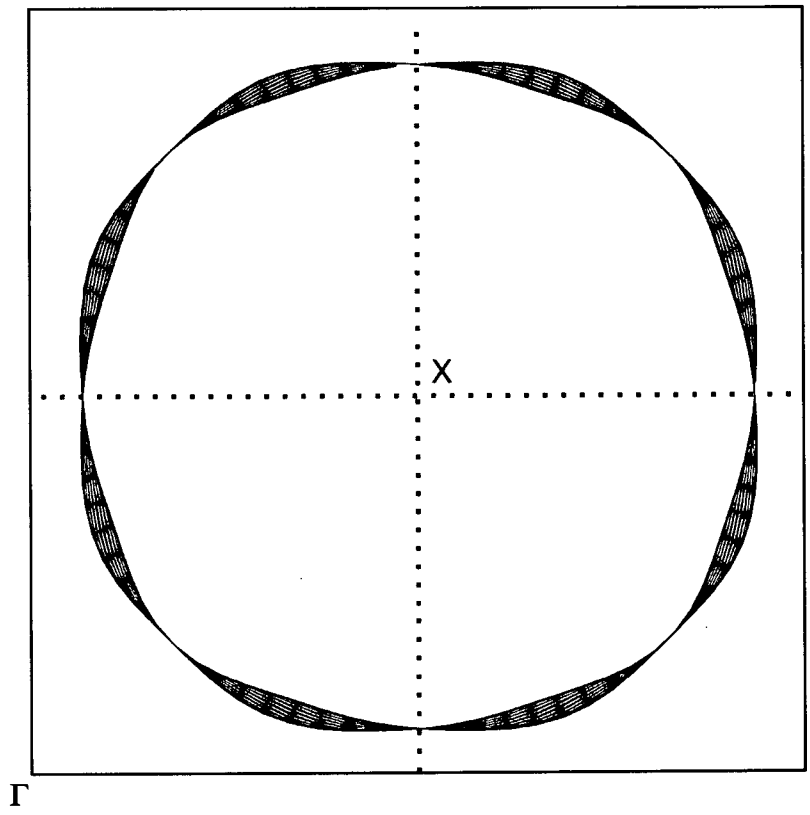

Figure 2.7: Projection of the AMRO FS onto the a-b plane for Tl2201. The magnitude of the c-axis warping has increased fourfold to emphasize the eight loci where $\mathbf{k_z}$ dispersion vanishes. (Reproduced from Hussey et al. [15])

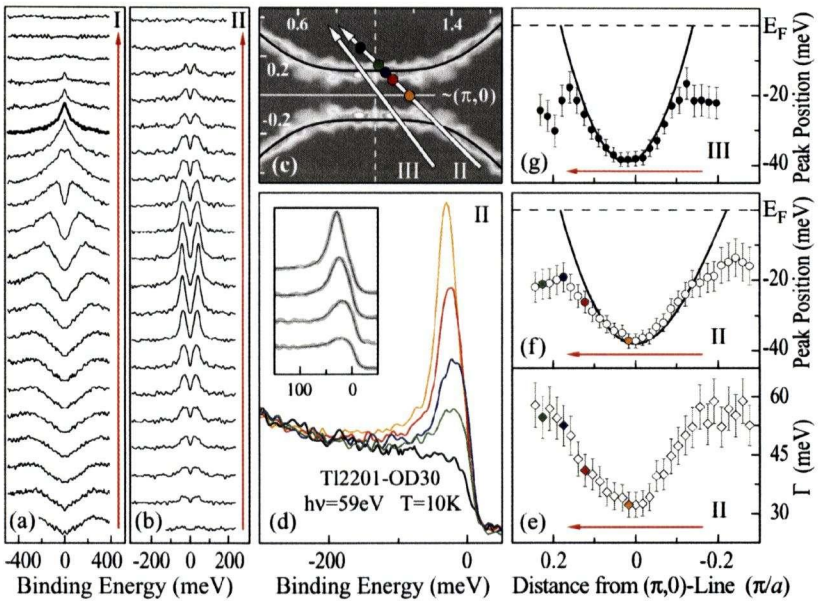

Figure 2.8: (a,b) Symmetrization of the ARPES spectra from along cut I and II shown in Figure 2.3. (c) Enlarged view of the FS of Tl2201-OD30 near $(\pi, 0)$. (d) Selected spectra from along cut II in (c); their k-space positions are indicated by circles of corresponding colour. (e,f) QP linewidth Γ and peak position from a Lorentzian fit of the energy distribution curves along cut II in (c). (g) QP peak position along cut III in (c). Black lines in (c,f,g) are the tight-binding results.

2.8b), which establishes the existence of the d-wave gap.

A more quantitative analysis of the gap was performed by fitting ARPES spectra from cuts that crossed the underlying normal state FS. The model used for the spectra was a Lorentzian QP peak plus a steplike background, determined from the ARPES spectra with $k \gg k_F$. This function was then multiplied by the Fermi function and convoluted with the instrumental energy resolution function to obtain the functional form that was fit to the data [8]. This procedure for determining the gap has been done for Bi2212 [26]. Figure 2.8d (inset) shows good agreement between the raw data and the fit. Since heavily overdoped cuprates have weaker electron correlations, the good agreement between the measured QP peak and the Lorentzian is not surprising.

Figures 2.8g and f show the peak positions from the fits compared with the tight-binding normal state dispersion, near the antinodal region. At higher binding energies, there is good agreement between the fit peak positions and the normal state dispersion. At lower binding energies, however, the QP peak does not reach E_F and instead reaches a minimum at $\Delta_P \simeq 17$ meV and disperses back to higher binding energy. This behaviour is a standard feature of Bogoliubov QPs. At the nodal region, the QP peak does cross E_F (not shown), while at intermediate momenta, a gap smaller than the one at the nodal region is observed.

The ARPES gap size is often determined by analyzing the LEM [8]. This procedure, however, is not robust at finite temperatures and finite instrument resolutions. The LEM is shown to vary rapidly and nonlinearly with both temperature and resolution. This effect has caused confusion, as the Fermi-Dirac distribution function for a metal is always equal to 1/2 at E_F, making the LEM of the angle-integrated photoemission spectrum exactly at E_F. Even for a metal, with ARPES spectra, the LEMs at different k-values will vary widely with temperature and instrument resolutions [27]. Further, the nature of these variations will be highly dependent on the details of the electronic dispersion and spectral lineshapes. An important consequence is that at k_F, the LEM is often well above E_F. Analysis on the change of the LEM as a function of temperature, lineshape, electronic dispersion, error in determining k_F and instrument resolution in Bi2212 has been performed and shows that the discrepancy between the LEM and the QP peak position is on the same order as the superconducting gap itself for typical experimental parameters, in the highly overdoped side of the phase diagram [27]. Results showing the evolution of the LEM with respect to experimental parameters is shown in Figure 2.9.

Despite the LEM gap not being as robust as the gap determined by QP peak position, the LEM gap was still determined for Tl2201-OD30 ($\Delta_{LE} \simeq 8$ meV), for comparison with LEM simulations. In fact, the difference between the two quantities ($\Delta_P \simeq 2\Delta_{LE}$) has been noted for other cuprates [8, 27].

2.2 Momentum evolution of quasi-particle lineshapes

The momentum evolution of the QP lineshapes depends on the strength and nature of the many-body effects present in the materials. The shape of ARPES energy distribution curves (EDCs), however, are affected by not only the band structure and correlation effects, but also the momentum and energy resolution of the analyzer, scattering, matrix element effects and the incoherent background. Providing a criterion for separating ARPES spectra into a QP lineshape and an incoherent background is a challenging task [28]. Nevertheless, it is possible to reduce the problems from matrix element effects by choosing appropriate experimental parameters, such that by subtracting a phenomenological ARPES background (determined from spectra at $k \gg k_F$) a sufficient QP peak can be isolated for a qualitative analysis of QP lineshape as a function of momentum. For this experiment, circularly polarized 59 eV photons were used. Circular polarization was chosen in order to minimize matrix element effects, which can be shown to be most extreme for linear polarization based on symmetry arguments [8]. The photon energy was chosen as a result of experience on other cuprates – specifically, $La_{2-x}Sr_xCuO_4$ (LSCO) where similar photon energies were used to reveal structure that had previously been unobservable in ARPES data [29]. In order to gain more reliable information, data was taken over multiple BZs, where it was observed that for the same point in the reduced zone scheme, lineshapes from different BZs were qualitatively very similar.

Turning our attention to the evolution of the lineshapes as a function of momentum, we see that in the nodal region, as has been previously observed in photoemission studies of the cuprates, the width of the QP peak increases as a function of binding energy (Figure 2.8b), as expected from simple phase-space arguments. This is in sharp contrast to the antinodal region, where the sharpest peak is found at the bottom of the band. The linewidth Γ of the QP peak is observed to grow from ~30 to ~55 meV as the QP peak disperses from ~39 to ~20 meV binding energy (see Figure 2.8e). Possible origins for this anomalous

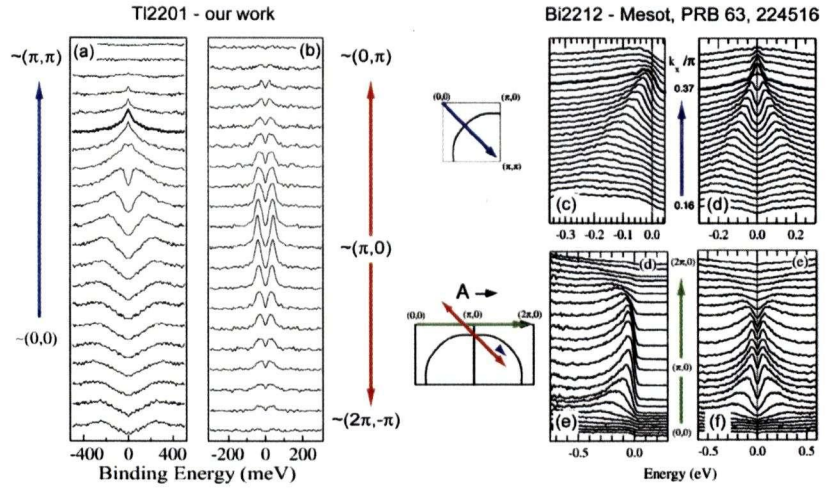

Figure 2.9: Temperature dependence of the model Bi2212 photoemission spectra with no gap included. (a–c) Electronic dispersion curves (EDCs) for temperatures ranging from 10 to 290 K with 20 K steps; narrowest EDCs corresponding to the lowest temperature. (d) LEM position as a function of temperature for different instrument momentum resolutions. (e) LEM position as a function of temperature for different instrument energy resolutions. (f) LEM position as a function of temperature for different positions in k. The lower curves filled with grey in panels (a) and (c) represent the temperature-dependent background for 10 and 290 K. The bold curves in panels (d)–(f) show the LEM for typical experimental parameters $R - \omega = 20$ meV, $R_k = 0.007$ Å, $k = k_F$. (Reproduced from Kordyuk et al. [27])

behaviour will be discussed later. Another striking feature of the lineshape evolution is that the QP peaks are much broader in the nodal region than in the antinodal region (see Figures 2.8a, b). Figure 2.10a presents a compilation of spectra along the FS contour, with k slightly smaller than k_F, corresponding to a binding energy of ~35 meV. This choice is dictated by the need to be sufficiently below E_F to have the spectra affected by neither the opening of the d-wave gap nor the anomalous low-binding-energy broadening depicted in Figure 2.8e. A sharp peak near $(\pi, 0)$ is seen to become progressively broader as $(\pi/2, \pi/2)$ is approached. In order to determine whether this apparent broadening represents an increase in the QP linewidth Γ or merely a loss of spectral weight, the momentum-independent background, taken from $k \gg k_F$, is subtracted from the ARPES spectra as shown in Figure 2.10b [8, 28]. Figure 2.10c shows the result of integrating the background spectra over varying energy ranges. When the QP peak is integrated over a small range, there is a drop as a function of FS angle; i.e., when integrated over a narrow energy window, the QP appears to lose weight in the nodal region. As the energy window of the integration region is expanded to 550 meV, however, the spectral weight of the QP peaks is seen to remain constant. This indicates that this k-dependent broadening is entirely due to a broadening of the QP spectrum rather than due to matrix element effects.

2.2.1 Significance of QP peak anisotropy

The observed QP anisotropy of Tl2201-OD30, with peaks much broader in the nodal than the antinodal region, is in sharp contrast with the behaviour observed in underdoped cuprates, where the QP peaks are sharp near $(\pi/2, \pi/2)$ and very broad around $(\pi, 0)$ in the normal state. As doping is increased, the antinodal QP peaks are observed to gain coherence, but they still remain significantly broader than the nodal peaks at optimal doping, creating the expectation that increasing doping will simply render the QP linewidths more isotropic. The QP peaks are seen to gain coherence at all momenta, but especially in the antinodal region, in the superconducting state. Even in the superconducting state, however, ARPES linewidths are still highly anisotropic, with a minimum at $(\pi/2, \pi/2)$ [8]. The reverse QP anisotropy observed in Tl2201-OD30 (Figure 2.11b), and a similar, albeit less pronounced, effect in Tl2201-OD63 (Figure 2.11a) indicate a trend with respect to doping. The notion that this trend may be generic in cuprates is suggested by recent ARPES results from $x = 0.22$

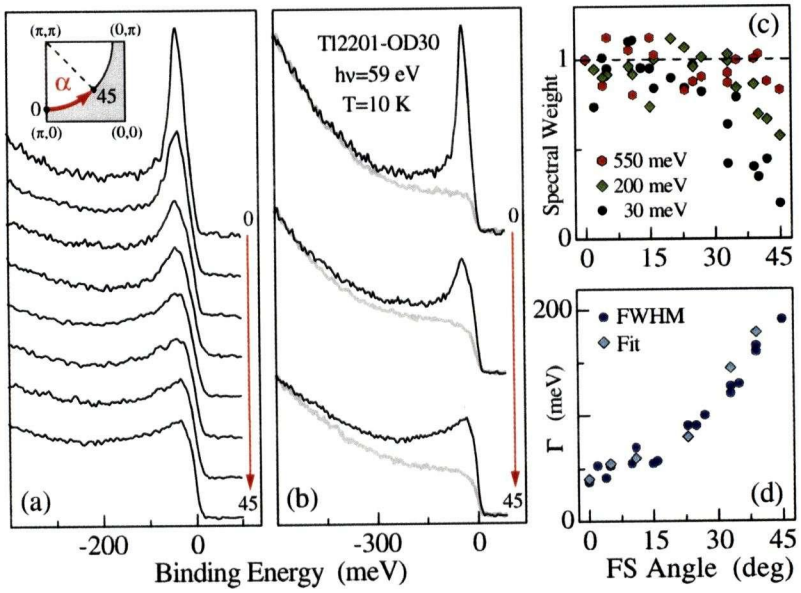

Figure 2.10: (a) Tl2201-OD30 ARPES spectra at k slightly smaller than k_F along the FS contour (corresponding to a peak position of ~35 meV). (b) Selected spectra from (a) along with corresponding $k \gg k_F$ background. (c) Spectral weight of background subtracted spectra integrated over different energy ranges vs. FS-angle α. (d) QP linewidth Γ vs. α.

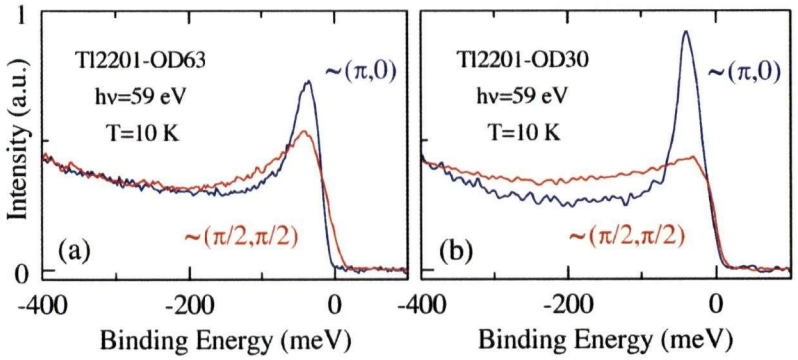

Figure 2.11: (a) Tl2201-OD63 and (b) Tl2201-OD30 spectra at $k \lesssim k_F$ in the nodal and antinodal regions.

LSCO [16, 17] showing a reverse QP anisotropy qualitatively similar to that seen in Tl2201-OD63. For both $x = 0.22$ LSCO and Tl2201-OD63, $T_c \simeq 2/3T_c^{\max}$.

Investigating quantum criticality and phase changes

The QP anisotropy reversal observed could be coincident with the proposed quantum critical point in the cuprate phase diagram [30]. It has been suggested that quantum phase transition from a $d_{x^2-y^2}$ to a $d_{x^2-y^2} + id_{xy}$ order parameter, as a function of some tuning parameter, possibly doping, may give rise to increased scattering rates of the nodal QPs. At the phase transition, low-energy bosonic modes would couple to the gapless nodal QPs [31]. While this proposal provides a convenient mechanism for explaining the broad QP lineshape in the nodal direction, a complex d_{xy} pairing component (i.e., $\sin k_x \sin k_y$) would generate an order parameter with no nodes. This is inconsistent with the results from Tl2201-OD30, which show a clear FS crossing in the nodal region. Heat transport measurements on Tl2201 indicate that the superconducting order parameter has nodes, and further, is consistent with the simplest $d_{x^2-y^2}$ pairing scenario [11]. The Tl2201-OD30 data, coupled with the heat transport data, provides strong evidence that quantum criticality, if it exists, is either not associated with the development of an id_{xy} order parameter, or that doping is not, in fact, the actual tuning parameter.

ARPES-specific broadening mechanisms

Magnetotransport experiments – where a small magnetoresistance and a weak T-dependence of the resistivity and cotangent of the Hall angle have been observed – do not indicate the presence of strongly k-dependent scattering rates. While these experiments are performed in the normal state, in contrast to the ARPES results presented, it may indicate that ARPES-specific scattering mechanisms for the nodal QPs, such as elastic forward scattering and the effects of a non-zero k_z dispersion, have to be examined.

The effect of elastic forward (small-angle) scattering due to n_i out-of-plane impurities, such as cation substitution and interstitial oxygen, on the ARPES spectra has been shown to be suppressed in cuprates in the superconducting state by a cancellation with an anomalous scattering process for states near the FS and away from the nodal direction. This anomalous scattering process vanishes in the nodal direction [32]. Elastic forward scattering contributes a term $\Gamma_{\mathbf{k_F}} \propto (n_i V_o^2)/(v_{\mathbf{k_F}} \kappa^3)$ to the normal state electronic scattering, in the limit of large κ^{-1}, where V_0 and κ^{-1} are the strength and range of the impurity potential, respectively [32]. While $\Gamma_{\mathbf{k_F}}$ is smaller at the nodes due to a larger Fermi velocity $v_{\mathbf{k_F}}$ above T_c, the superconducting state displays the opposite behaviour due to cancellation between the normal state scattering and the anomalous scattering. After this cancellation is taken into account, the forward scattering rate is reduced by a factor of $\sqrt{\omega^2 - \Delta_{\mathbf{k}}^2}/|\omega|$, for $|\omega| \gtrsim |\Delta_{\mathbf{k}}^2|$ [32]. This behaviour is not unexpected, as below T_c, $\Gamma_{\mathbf{k_F}}$ must be suppressed for electron energies smaller than the gap size, to conserve energy. In the nodal direction, however, the forward scattering is still pair-breaking, and no suppression of scattering rates is expected. This reduction in the forward scattering varies smoothly from no reduction in the nodal region to a strong suppression of the effects of forward scattering in the antinodal region, consistent with the observed trend. While forward scattering may explain why a strong reverse anisotropy of low-energy QP widths is seen in seen in the ARPES data presented, it does not explain the origin of the anomalous broadening of the QP lineshape as a function of binding energy observed in the nodal direction.

AMRO measurements indicate that the FS of Tl2201 has a coherent, albeit weak, 3D structure [15]. Data analysis on ARPES spectra from cuprates is normally based on the assumption of a true 2D FS, neglecting the small c-axis dispersion. In a true 2D system, spectral features are not affected by the photon energy other than through changes in the scattering rates and matrix

elements. This feature is in sharp contrast to 3D systems, where the location and shape of spectral features change as a function of photon energy due to momentum conservation requirements. It is precisely momentum conservation, and a knowledge of the band structure of the unoccupied levels, that allow, in principle, the determination of the 3D FS by measuring spectra over a range of photon energies [7]. However, it has been shown that finite lifetimes in the unoccupied bands result in the ARPES FS crossings being spread over the projection of the FS onto the $a-b$ plane at all photon energies, for realistic unoccupied band lifetimes [33]. Case studies on various HTSCs are presented by Markiewicz et al. [34]. The projection of the AMRO FS onto the a-b plane (Figure 2.7) reveals that at both the nodal and antinodal regions, there is no $\mathbf{k_z}$ dispersion. Thus, by the analysis of Bansil et al. [33], the k_z dispersion should not affect the QP lineshape at either the nodal or the antinodal region, indicating that if the 3D character is responsible for the anomalous broadening of the nodal region QP peak as a function of binding energy or the nodal-antinodal reverse anisotropy, then the mechanism is not at all obvious.

Another candidate for explaining the anomalous behaviour of this system is microscopic inhomogeneity. It has been shown through STM measurements that on Bi2212, there is a strong inhomogeneity in the local density of states (LDOS) [35]. It is suggested by Pan et al. [35] that the the inhomogeneity in the bulk may give rise to a microscopic modulation in the gap size, and further, that averaging over a macroscopic spot on the sample, as is effectively done by ARPES, will produce a broadening in the antinodal region and will have little effect in the nodal region. Pan et al. [35] use this observation to explain the lineshape anisotropy around the FS in underdoped and optimally-doped cuprates. By analogous reasoning, microscopic inhomogeneity may be responsible for the observed broadening of the antinodal QPs towards lower binding energies.

2.3 Conclusion

ARPES data taken on overdoped Tl2201 indicate two anomalous features. In the nodal region, the QP linewidths increase as binding energy is decreased. This is in contrast to what is expected from previous photoemission studies on optimally and underdoped cuprates, and from phase space arguments. The QP lineshapes are seen to be broader in the nodal regions than in the antinodal re-

gions, in contrast to optimally and underdoped cuprates. The trend seen from comparing Tl2201-OD30 and Tl2201-OD63, together with previously reported LSCO data, suggest that the anisotropy reversal may be a generic feature of the cuprates. More measurements, especially with respect to temperature dependence and over a larger range of dopings, as well as theoretical work, is needed to properly interpret the trends seen from this experiment. Equally importantly, Tl2201 has been demonstrated to be an suitable system for single-particle spectroscopic studies of the intrinsic properties of the doped CO_2 plane. Future Tl2201 ARPES and scanning tunnelling microscopy work promises to progress our understanding of HTSCs, especially in the overdoped side of the phase diagram.

Chapter 3

Construction of a new ARPES system

An in-house ARPES system is being constructed at UBC with the goal of improving both energy resolution (to 1.5 meV) and angular resolution (to 0.2°), with the highest possible sample positioning accuracy. This system is being designed to be coupled directly to an MBE such that samples can be grown and passed directly into the ARPES cyrostat without ever being exposed to pressures higher than 5×10^{-10} mbar. Connection to the MBE will allow ARPES to be done on the vast array of crystal structures that can be grown by MBE, rather than on the small range of crystals that can be cleaved in vacuo. CaO and NiO films, with the introduction of appropriate specific point defects, will be used to generate half-metallic ferromagnets and antiferromagnets, represent a new class of magnetic systems, and will be synthesized and studied, for instance. Since the samples grown by MBE are inherently thin films, systems with much higher resistivities will be able to be studied without the charging problems found in bulk crystals, so long as a conductive substrate is used.

Beyond the advantages offered by a broader range of samples available for study, the MBE-grown samples offer a tuning parameter not available in single crystals – namely, the lattice constants. By choosing substrates with varying lattice constants, the strain, bond lengths and bond angles of the grown samples are varied accordingly. This allows the lattice constants on the thin films grown to be treated as an additional tuning parameter. In ARPES studies of single crystals, there is always a complication in the interpretation of the results due to the difficulty in separating the spectral components associated with the bulk states from those of the surface states. This difficulty is resolved in studies on thin films, as the concepts of bulk states and surface states are ill-defined in the limit of thin samples; all electronic states of the film are accessible from the surface, and all surface states effectively permeate the entire sample, provided

the film is only a few unit cells thick.

3.1 Elements of the new ARPES system

The fundamental components of an ARPES system are an electron analyzer, a monochromatic photon source and a cryostat, which has to be designed both to bring the sample to the desired temperature and to be able to accurately move and rotate the sample. While analyzer resolutions, cryostat temperature monitoring accuracy, cryostat angle-setting accuracy and photon source linewidth set a limit on the accuracy of ARPES measurements by the system, the measurements can easily be compromised by a number of other factors, such as the thermal contact between the cold head of the cryostat and the sample itself, the quality of the vacuum, and, most importantly, residual electric and magnetic fields inside the analysis chamber, particularly those that vary in time. Introducing the MBE to the system provides another design challenge in that the sample grown in the MBE must be able to be passed to the cryostat without exposing the grown surface to any contaminants. The design constraints used in designing each of these components are addressed.

3.2 Electron analyzer

To determine the energy and angle of photoelectron emission, a hemispherical analyzer [36] – the Phoibos 150 CCD manufactured by SPECS – was chosen. The hemispherical analyzers used in modern ARPES experiments differ from those described in Moore et al. (2003) in that they have electrostatic lenses in front of the entrance slit, which are used both to change the energy of the incoming electron, and to Fourier transform the incoming electron spectrum, focusing emitted at a given angle and energy to a unique location on the detection plane, regardless of the location of electron emission. The other major difference is that analyzers used in ARPES have a 2D electron detector, consisting of a double-layer multichannel plate (MCP) [36] to amplify the electron signal, followed by a phosphor screen, onto which the electrons emitted from the MCP are accelerated. Light generated by the electrons hitting the phosphor screen is detected by a CCD camera. The implementation of a 2D electron detector allows energies moderately above and below the pass energies, as well as electrons coming in at angles off normal to be detected. Thus, the energy and emission

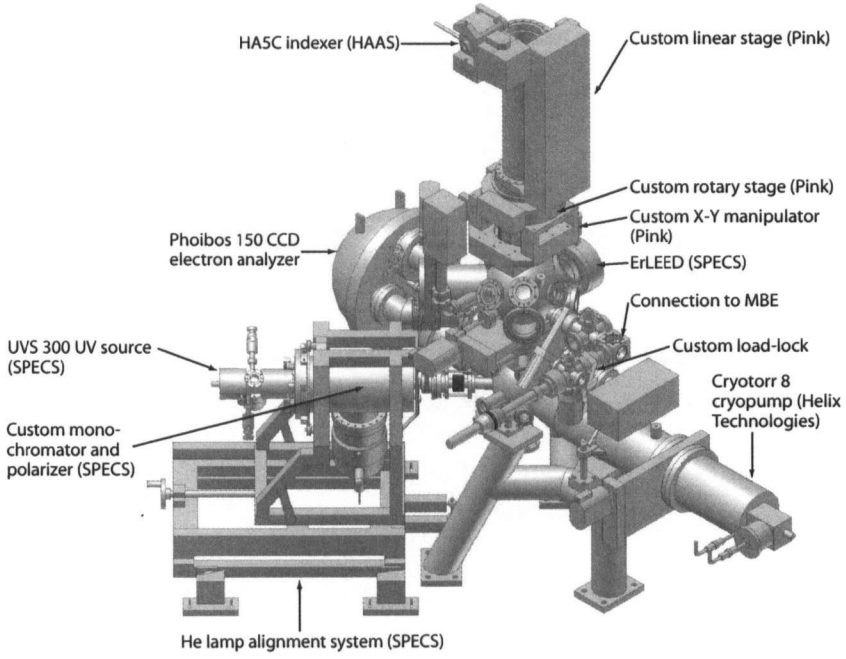

Figure 3.1: The UBC ARPES system (cryostat and transfer system not shown).

angle of an electron can be determined by the position where it is detected.

The Phoibos 150 CCD has recently emerged as a competitive high-resolution electron analyzer. While it has yet to be used for ARPES studies on cuprates, the Phoibos 150 presents several advantages. The Phoibos 150, uses a double layer of μ-metal shielding to screen external magnetic fields, and uses titanium fasteners, which do not display ferromagnetism regardless of their history, inside the analyzer body to ensure that the lowest possible residual magnetic fields are maintained. Another major advantage of the Phoibos 150 is the use of machined hemispheres, as compared to the traditional formed hemispheres. Formed parts have much lower tolerances than machined parts [37], and introduce anisotropic strain in the formed metal [38], which can allow formed parts to deform as they stress-relieve over time, thus degrading analyzer accuracy.

A unique feature of the SPECS analyzers is the approach taken with regards to interpretation of the positions of electrons detected on the 2D detector. This position, in general, is a nonlinear function of electron energy and angle, and this function changes as the pass energy and energy window of the analyzer are varied. The Phoibos 150 CCD is supplied with software that allows the characterization of the analyzer response function. This response function is inverted, allowing the SPECS software to return an intensity plot with angle and energy as linear and orthogonal coordinates. This procedure greatly simplifies analysis of the data, and is done in real time such that the experimenters can see clearly what they are measuring.

3.2.1 Analyzer resolution

Test reports for our Phoibos 150 CCD electron analyzer show an ultimate angular resolution of 0.11° and an ultimate energy resolution of 1.0 meV. Since analyzer resolution is strongly affected by stray electric and magnetic fields within the analysis chamber, the analyzer was tested in our analysis chamber, in its final mounting position, to ensure that the measured resolution can in fact be realized in practice.

The testing apparatus for angular resolution consisted of an electron gun, a stainless steel target and a slit array. Electrons emitted from the surface of the target pass through a slit array and into the analyzer. The slits have a width of 100 μm and are placed 35 mm from the target, corresponding to an angular opening of 0.16°. The FWHM of the beam from the SPECS EQ 22/35 electron gun is reported to be as small as 50 μm, corresponding to an angle of 0.08°, but

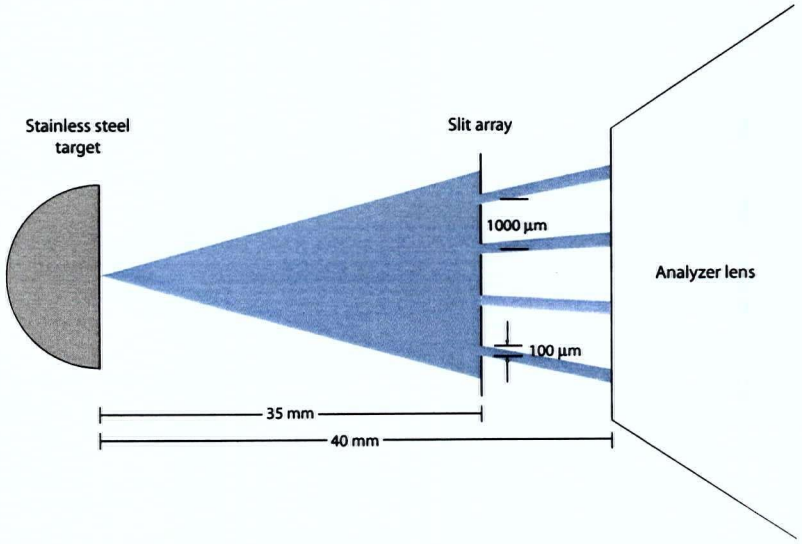

Figure 3.2: Schematic diagram depicting the analyzer angular resolution test apparatus.

measuring the electron spot size at the time of testing was not possible. The smallest FWHM for the image of the slit detected by the analyzer during testing was 0.21°. Subtracting the contributions to this measured angular width due to the minimum electron spot size and the slit width gives an analyzer electron resolution of 0.11° according to the following equation:

$$FWHM_{\text{angular resolution}} = \sqrt{FWHM^2_{\text{measured angle}} - FWHM^2_{\text{slit width}} - FWHM^2_{\text{electron spot}}}.$$

Note that this value represents an upper limit for $FWHM_{\text{angular resolution}}$, since, without a direct measurement of the spot size from the electron gun, it is impossible to know with certainty that the gun was optimized to produce the reported minimum spot size.

To produce monochromatic electrons for the energy resolution test, Xe atoms were bombarded with a He emission. The He lines have a FWHM of 1.0 meV, and Doppler broadening of the Xe target gas introduces a 3.3 meV width to the

emitted electrons. Considering the contributions of the He and Xe widths, the FWHM of the emitted electron linewidth as measured by the Phoibos 150 CCD of 3.6 meV corresponds to an analyzer energy resolution of 1.0 meV, as a result of the following equation:

$$FWHM_{\text{energy resolution}} = \sqrt{FWHM^2_{\text{measured angle}} - FWHM^2_{\text{He UV source}} - FWHM^2_{\text{Doppler}}}.$$

This calculation, however, does not take into account the stray electric and magnetic fields produced by the Xe gas cell. The gas cell confines the Xe electromagnetically, producing oscillation fields, which are detrimental to the analyzer resolution. The gas cell is designed such that these fields can be effectively cancelled outside of the gas volume, but the photoelectrons emitted from the Xe still need to pass through some region with oscillating fields before they leave the gas cell. As a result, the 1.0 meV quoted represents an upper bound on the true value of $FWHM_{\text{energy resolution}}$.

The impressive results of these tests not only indicate the potential of the Phoibos 150 CCD for ARPES studies, but demonstrate good shielding by the μ-metal analysis chamber.

3.3 Cryostat and manipulator

The cryostat and manipulator present major design challenges. The ideal cryostat and manipulator combination allows the sample to be accurately positioned, with three spatial and three angular degrees of freedom, at an arbitrary temperature, without introducing any stray electric or magnetic fields and without contaminating the vacuum.

Existing ARPES cryostats consistantly depart from this ideal in two important ways. First, the thermal contact between cold head and the sample is weak in two areas: the cold head and the rotating piece that holds the sample post is usually thermally linked through gears and copper braids, resulting in a poor thermal contact, and the clamping of the sample post to the piece that holds it is not typically sufficiently forceful to ensure good conductivity. Second, the rotation of the sample-post holder typically introduces a degree of angular uncertainty much larger than the instrument resolution, and differential thermal

expansion alters these angles as sample temperature is changed. The difficult task of avoiding these difficulties has been addressed through a joint initiative between the UBC ARPES group and Quantum Technologies, a Vancouver-based scientific instrument manufacturing firm specializing in cryogenics.

To ensure good thermal contact between the cold head and the sample, the sample holder is clamped directly to the cold head, necessitating a rotating cold head. This unconventional design feature presents challenges, but its realization will result in much more robust temperature control and lower ultimate sample temperatures. To address the problem of sample positioning, a computer-numeric control (CNC) indexer is used to operate a parallelogram-style actuator that sets the sample angle, with ball-bearing pivots to eliminate hysteresis in angle-setting.

As well as ensuring intrinsic mechanical accuracy of the cryostat, it is important to ensure that this accuracy not be degraded by allowing either deformation of the chamber, as a result of changing cryostat positions, or vibrations from the cryopump, to affect positioning accuracy. In order to ensure the rigidity of the chamber, only spherical and cylindrical elements are used in its construction. To block vibrations from the cryopump, the frame for the chamber is constructed from 125 mm diameter aluminum rod.

A flow cryostat and manipulator for the UBC ARPES system has been designed and is under construction. The coordinate convention followed in the description of the cryostat is as follows: the x and y axes are parallel to the ground. x represents translation perpendicular to the analyzer lens, while y represents translation along the axis of the analyzer lens. z represents vertical translation. ϕ represents rotation about the z-axis; the sample is normal to the analyzer when $\phi = 0$. x, y, z and ϕ motion are controlled with the x-y stage manufactured in-house and with custom ϕ and z stages manufactured by Pink Vacuum. θ represents rotation about the x-axis when $\phi = 0$, and the θ axis rotates with ϕ. ω represents rotation about the normal to the sample, and hence, the ω-axis rotates with both θ and ϕ. θ rotation is controlled by a CNC indexer, manufactured by HAAS, while ω rotation is accomplished manually. θ and ϕ are meant to be actuated continually during measurements, while ω is meant to define the orientation of the sample, and thus is set at the beginning of a measurement (see Figure 3.3).

Cryostat cooling is provided by liquid helium. Liquid He enters the cryostat through a transfer line into a phase separator. Helium gas is exhausted from the top of the phase separator, where it is used to cool the heat shield, and

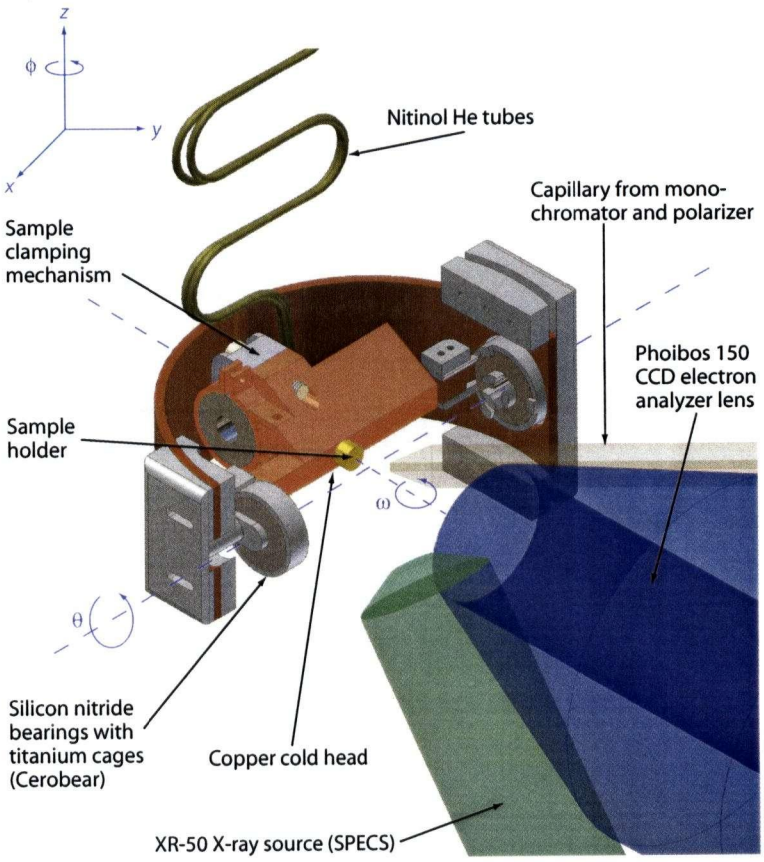

Figure 3.3: Cryostat schematic and coordinate system.

exits the system. Liquid He leaves the bottom of the phase separator, through a flow-controlling needle valve and travels to the rotating cold head via a flexible tube. Exhaust He gas from the cold head is returned via a second flexible tube.

3.3.1 Cryostat materials

The constraints of UHV-compatible materials and materials that do not generate stray electric and magnetic fields greatly limit the choice of materials for the cryostat. UHV-compatible engineering materials are restricted to a few types of glass, some metals, some ceramics and a small number of other materials [36]. Furthermore, of the UHV-compatible metals appropriate for dynamic contact, which is needed for the angular positioning of the samples, most not ferromagnetic at room temperature undergo a ferromagnetic transition as they cool to temperatures appropriate for ARPES measurement, precluding their use. On top of these constraints, materials chosen must have the right thermal properties – either good conducting or insulating behaviour – depending on their locations. Further, the thermal expansion coefficients of candidate materials must be considered to ensure that the system is not distorted as the cryostat temperature changes, to prevent deformation and failure of components, and to ensure that the sample position and angle are not affected by adjustments in temperature.

Away from the cold head, temperatures are not as low, and therefore, ferromagnetic transitions are less likely, and the presence of small magnetic moments is acceptable. Thus, for system components away from the cold head, 316 stainless steel and UNS C10200 oxygen-free electronic copper were chosen for their vastly different thermal conductivities [39], with UNS C10200 having a thermal conductivity at all relevant temperatures more than 1000 times greater than 316. Further, the coefficients of thermal expansion of these materials are matched to within 10% at all relevant temperatures [40].

Near the cold head, temperatures are sufficiently low that stainless steel would undergo a magnetic transition if it were used; thus, it must be abandoned as a material choice. UNS C10200 is also abandoned in favour of the higher-purity alloy UNS C10100, as the conductivity near the sample is more critical. Titanium, 7075-T6 aluminum alloy and beryllium-copper are all used for smaller high-strength components in this area.

The tubes carrying liquid He to the cold head endure a 3% deformation as the θ angle is cycled. Very few metals have a significant fatigue life under

such strains. Further, most materials become more brittle as they are cooled from room temperature. Worse, the best spring materials are almost all steels, and thus are not usable due to their magnetism [41]. Fortunately, nitinol, a superelastic shape-memory nickel-titanium alloy, was found not only to meet, but to greatly exceed the design requirements. When nitinol is cooled below its transformation temperature to its martensite phase, it can undergo 10% deformation without any irreversible changes. Nitinol becomes more resistant to fatigue as it is cooled. While data is not available at cryogenic temperatures, higher-temperature fatigue lifetimes of over 30000 cycles are reported for 3% strain. Given the rapid increase in fatigue life as the test temperature is reduced, it is reasonable to expect a fatigue life of over 10^7 cycles at typical measurement temperatures. Nitinol is also thermoformable, allowing the the desired tube shape to be fabricated in-house in an atmosphere-controlled furnace. Further, thermoforming temperatures between 300–500°C increase the transformation temperature, resulting in better fatigue lifetimes at room temperature [42]. Measurements of magnetic properties of nitinol at cryogenic temperatures are not available in the literature. Thus, the magnetic properties of nitinol down to 2 K were investigated with a superconducting quantum interference device (SQUID). Minimal ferromagnetism was detected at these temperatures, and it was calculated to be insignificant compared to other stray magnetic fields in the chamber. It was not clear whether the origin of the ferromagnetism was intrinsic to the nitinol, the result of nickel inclusions, or due to ferromagnetic contaminants in the SQUID.

The bearings used for the θ rotation also presented demanding material constraints. To maintain UHV compatibility, the bearings cannot be lubricated. This restriction already presents a challenge for the bearing material, as vacuum galling and cold-welding occur readily without lubrication [36]. Further, the bearings have to provide a reliable thermal break between the heat shield on which they are mounted, which is maintained at ~100 K, and the cold head, which is designed to cycle between 2 and 300 K. The bearings must also be able withstand the differential thermal expansion between the inner and outer races at different temperatures. On top of these requirements, the bearing must also be non-magnetic. Si_3N_4 ceramic is used as a bearing material for applications requiring resistance to thermal shock, and is non-magnetic, although it does have a high thermal conductivity. Nonmetals do not suffer from the galling and cold-welding problems faced by metallic bearing surfaces, and outgassing in ceramics is generally not a problem [36]. In vacuum, however, the bulk of

the thermal resistance of composite objects is often due to the thermal contact between components. Engineering surfaces are never perfectly flat, and as a result, contact between two solid surfaces pressed together only takes place over a few small spots. For this reason, at low temperatures (where thermal radiation is not a dominant source of heat transfer) the conductance between mating surfaces depends on the size and number of these small contact points, which in turn depends on the pressure between the two surfaces. Conductance across solid interfaces is thus highly dependent on the clamping pressure. The conductance is found to depend approximately linearly on pressure [43]. Si_3N_4 ceramic is extremely hard (80 Rockwell C), so it is not unreasonable to expect the contact area, and hence the thermal conductivity, between two Si_3N_4 mating surfaces to be small despite the high thermal conductivity of the bulk material. With this line of reasoning in mind, the heat flow across a Si_3N_4 608 bearing with an inner and outer races at 66 and 4 K, respectively, was measured, and found to be 10 mW, rendering the heat load from the bearings much less than the calculated heat load from thermal radiation. Custom Si_3N_4 607 ball bearings with titanium cages have been ordered from Cerobear for construction of the cryostat.

3.3.2 θ angle manipulation

The θ angle is set by a HAAS HA5C CNC indexer, which has a positioning accuracy of 0.008°. The top bar of the parallelogram and the indexer are mounted on top of the manipulator, outside of the vacuum. The moving vertical parallelogram arm is coupled to the vacuum space by edge-welded bellows, while the cryostat body and heat shield act as the stationary arm. The cold head itself acts as the lower parallelogram arm. The coefficients of thermal expansion of the vertical parallelogram arms are matched, and the arms are thermally tied together in numerous places to ensure matching temperatures, thereby removing differential thermal expansion problems from the vertical arms of the parallelogram. The temperature of the cold head is monitored accurately as part of the temperature-control feedback system, allowing corrections to the indexer angle due to differential expansion of the upper and lower arms to be calculated and monitored on the fly. Analysis of the angular error caused by bearing clearances and differential thermal expansion not already taken into account are non-trivial, but even the most conservative analysis indicates that it is irrelevant compared to the angular resolution of the analyzer.

3.3.3 z translation

z-motion is accomplished by a relatively standard manipulator. The differences between stock manipulators and the custom z-stage manufactured by Pink is mainly size. In order to minimize bending of the cryostat from uneven heat loads and to hold the complex ϕ manipulation system, a comparatively large diameter of 100 mm was chosen for the cryostat, which necessitated a larger z-stage. Further, the 21.8 kg mass of the CNC indexer, hanging over the edge of the manipulator, is large enough to distort the stock manipulators and degrade the angle-setting accuracy. Two massive 40 mm columns provide the Pink manipulator with the necessary stiffness. The z-stage is equipped with a linear scale to allow computerized motion control.

3.3.4 ϕ rotation

Due to the size and weight requirements imposed by the CNC indexer and the z-stage, the ϕ rotation stage requires a larger bore and greater mechanical strength than standard rotation stages. Unlike normal rotation stages, where the load is placed on the seals, resulting in rapid seal-wear, high rotation forces and limited load-bearing capacity, the bearing force of the Pink stage is supported by a 220-mm-diameter 4-contact ball-bearing. The ϕ stage is also equipped with a linear scale for computerized motion control.

3.3.5 x-y translation

The x-y motion is manually actuated. Like the z and ϕ stages, it is larger than commercially available stages. It is also equipped with linear encoders, although they are not used for feedback. In order to accommodate the larger stresses as a result of the large off-axis load and the vacuum pressure from the larger-area bellows, crossed cylindrical linear bearings are used, and in order to provide more robust and backlash-free positioning, ball-screws and ball-nuts are employed [44].

3.3.6 Sample mounting and ω rotation

Samples are mounted on a copper "bullet." The bullet must be grabbed from the rear by the sample transfer system, as surfaces grown by MBE are rapidly degraded if they face moving sample manipulation equipment. The cold head has a hole bored through it, into which the bullet is inserted. Holding the sample

from the rear necessitates a cryostat that will accept samples from the rear. While this presents some design challenges, it also offers unique opportunities. Having an unobstructed view of the front of the sample allows the use of low-energy electron diffraction (LEED) to monitor the orientation of the sample while the sample is rotated from the rear, allowing accurate sample positioning. Further, mechanisms for firm clamping and retraction of the bullet into the cold head can be mounted to the back of the cold head without interfering with electron trajectories.

3.3.7 Temperature control

Diode temperature monitors are attached to the cold head and to the inside of the phase separator, which also contains a liquid-level sensor. Non-inductively wound heaters are located inside the phase separator and on the cold head. Below 4 K, the phase separator is filled with liquid, and only the heater on the cold head is used to control the temperature. The helium exhaust is pumped on in order to the reduce the liquid temperature to 2 K. At higher temperatures, liquid helium entering the cold head could undergo explosive boiling, resulting in temperature instability. Thus, above 4 K, the heater in the phase separator is used to eliminate liquid helium such that cooling of the cold head is done by gaseous helium.

3.4 Helium lamp and monochromator

The UBC system uses a helium lamp as its UV source. The source used is the UVS 300, manufactured by SPECS. The UVS 300 can produce a photocurrent of 200 nA and has a linewidth of 1 meV. Photons from the UVS 300 enter a custom polarizing monochromator, also made by SPECS. The unique feature of the SPECS monochromator is that it allows rotation of the polarization, which is extremely valuable in ARPES studies due to the polarization dependence of the matrix elements. In order to expose the sample to maximal intensity, the photons from the monochromator are conveyed via a copper capillary to within 5 mm of the sample. The interior of the capillary is elliptical, to preserve polarization.

The UV source system must be aligned to allow the photon spot to coincide with the analyzer focus. Given the impressive mass ($\sim$300 kg) of the system, the frame holding the lamp must be able to actively position the lamp, and

the motion must correspond to rotations about the centre of the flex coupling between the chamber and the UV source. A frame with these features has been designed in collaboration with SPECS, and has been manufactured by SPECS.

3.5 Conclusion

The UBC ARPES system is expected to be a unique and powerful tool. Combining an MBE with an ARPES system allows a much wider range of materials to be studied, compared with a conventional ARPES system. In order to achieve the required mechanical and thermal precision, several novel design features have been introduced, including the use of a rotating cold head, allowing direct thermal contact to the sample holder, the introduction of thermoformed nitinol tubing to allow non-magnetic UHV-compatible transfer of liquid helium to the cold head, and the use of Si_3N_4 ball-bearings as both a non-magnetic, UHV-compatible pivot point capable of operating at low temperatures, and as a thermal break. With excellent analyzer resolution, the ability to rotate polarization and a mechanically and thermally accurate cryostat with a broad temperature range extending to 2 K, the new ARPES system will allow MBE-grown samples to be studied, which could produce important results for correlated systems in general, including HTSCs.

Bibliography

[1] Ian Falconer. *Olivia Saves the Circus.* Simon and Schuster, New York, 2001.

[2] Werner Holzwarth and Wolf Erlbruch. *The Story of the Little Mole Who Knew It Was None of His Business.* David Bennet Books, London, 1994.

[3] J. G. Bednorz and K. A. Muller. Possible high T_c superconductivity in the Ba-La-Cu-O system. *Z. Phys. B: Condensed Matter*, 64:189, 1986.

[4] Neil W. Ashcroft and N. David Mermin. *Solid State Physics.* Brooks/Cole, Pacific Grove, CA, 1976.

[5] Harald Ibach and Hans Lueth. *Solid-State Physics.* Springer, Berlin, 1995.

[6] J. Orenstein and A. J. Millis. Advances in the physics of high-temperature superconductivity. *Science*, 288:468–474, 2000.

[7] Stefan Huefner. *Photoelectron Spectroscopy.* Springer, Berlin, 1995.

[8] Andrea Damascelli, Zahid Hussain, and Zhi-Xun Shen. Angle-resolved photoemission studies of the cuprate semiconductors. *Reviews of Modern Physics*, 75:473–541, 2003.

[9] H. He, P. Bourges, Y. Sidis, C. Ulrich, L. P. Regnault, S. Pailhes, N. S. Berzigiarova, N. N. Kolesnikov, and B. Keimer. Magnetic resonant mode in the single-layer high-temperature superconductor $Tl_2Ba_2CuO_{6+\delta}$. *Science*, 295:1045–1047, 2002.

[10] H. Eisaki, N. Kaneko, D. L. Feng, A. Damascelli, P. K. Mang, K. M. Shen, Z.-X. Shen, and M. Geven. Effect of chemical inhomogeneity in bismuth-based copper oxide superconductors. *Physical Review B*, 69:064512, 2004.

[11] Cyril Proust, Etienne Boaknin, R. W. Hill, Louis Taillefer, and A. P. Mackenzie. Heat transport in a strongly overdoped cuprate: Fermi liquid and a pure *d*-wave BCS superconductor. *Physical Review Letters*, 89:147003, 2002.

[12] Y. Shimakawa, Y. Kubo, T. Manako, and H. Igarashi. Neutron-diffraction study of $Tl_2Ba_2CuO_{6+\delta}$ with various T_c's from 0 to 73 K. *Physical Review B*, 42:10165–10171, 1990.

[13] M. R. Norman. Magnetic collective mode dispersion in high-temperature superconductors. *Physical Review B*, 63:092509, 2001.

[14] C. C. Tsuei, J. R. Kirtley, Z. F. Ren, J. H. Wang, H. Raffy, and Z. Z. Li. Pure $d_{x^2-y^2}$ order-parameter symmetry in the tetragonal superconductor $Tl_2Ba_2CuO_{6+\delta}$. *Nature*, 387:481–483, 1997.

[15] N. E. Hussey, M. Abdel-Jawad, A. Carrington, A. P. Mackenzie, and L. Ballcas. A coherent three-dimensional Fermi surface in a high-transition-temperature superconductor. *Nature*, 425:814–817, 2003.

[16] T. Yoshida, X. J. Zhou, T. Sasagawa, W. L. Yang, P.V. Bogdanov, A. Lanzara, Z. Hussain, T. Mizokawa, A. Fujimori, H. Eisaki, Z.-X. Shen, T. Kakeshita, and S. Uchida. Metallic behavior of lightly doped $La_{2-x}Sr_xCuO_4$ with a Fermi surface forming an arc. *Physical Review Letters*, 91:027001, 2003.

[17] X. J. Zhou, T. Yoshida, D.-H. Lee, W. L. Yang, V. Brouet, F. Zhou, W. X. Ti, J. W. Xiong, Z. X. Zhao, T. Sasagawa, T. Kakeshita, H. Eisaki, S. Uchida, A. Fujimori, Z. Hussain, and Z.-X. Shen. Dichotomy between nodal and antinodal quasiparticles in underdoped $(La_{2-x}Sr_x)CuO_4$ superconductors. *Physical Review Letters*, 92:187001, 2004.

[18] D. C. Peets, Ruixing Liang, D. A. Bonn, W. N. Hardy, and M. Raudsepp. Growth of orthorhombic Tl-2201 single crystals by the self-flux method. *not published*, cond-mat:0211028v1, 2002.

[19] D. R. Hamann and L. F. Mattheiss. Electronic band properties of $Ba_2Tl_2CuO_6$. *Physical Review B*, 38:5138–5141, 1988.

[20] A. Damascelli, D. H. Lu, K. M. Shen, N. P. Armitage, R. Ronning, D. L. Feng, C. Kim, and Z.-X. Shen. Fermi surface, surface states and surface reconstruction in Sr_2RuO_4. *Physical Review Letters*, 85:5194–5197, 2000.

[21] H. Matsui, T. Sato, S.-C. Wang, H.-B. Yang, H. Ding, T. Fujii, T. Watanabe, and A. Matsuda. BCS-like Bogoliubov quasiparticles in high-T_c superconductors observed by angle-resolved photoemission spectroscopy. *Physical Review Letters*, 90:217002, 2003.

[22] A. P. Mackenzie, S. R. Julian, D. C. Sinclair, and C. T. Lin. Normal-state magnetotransport in superconducting $Tl_2Ba_2CuO_{6+\delta}$ to millikelvin temperatures. *Physical Review B*, 53:5848–5855, 1996.

[23] David J. Singh and Warren E. Pickett. Electronic characteristics of $Tl_2Ba_2CuO_6$–Fermi surface, positron wavefunction, electric field gradients, and transport parameters. *Physica C*, 203:193–202, 1992.

[24] J. Mesot, M. Randeria, M. R. Norman, A. Kaminski, H. M. Fretwell, J. C. Campuzano, H. Ding, T. Takeuchi, T. Sato, T. Yokoya, T. Takahashi, I. Chong, T. Terashima, M. Takano, T. Mochiku, and K. Kadowaki. Determination of the Fermi surface in high T_c superconductors by angle-resolved photoemission spectroscopy. *Physical Review B*, 63:224516, 2001.

[25] M. R. Norman, H. Ding, M. Randeria, J. C. Campuzano, T. Yokoya, T. Takeuchi, T. Takahashi, T. Mochiku, K. Kadowaki, P. Guptasarma, and D. G. Hinks. Destruction of the Fermi surface in underdoped high-T_c superconductors. *Nature*, 392:157–160, 1998.

[26] H. Ding, M. R. Norman, J. C. Campuzano, M. Randeria, A. F. Bellman, T. Yokoya, T. Takahashi, T. Mochiku, and K. Kadowaki. Angle-resolved photoemission spectroscopy study of the superconducting gap anisotropy in $Bi_2Sr_2Ca_1Cu_2O_{8+\delta}$. *Physical Review B*, 54:9678, 1996.

[27] A. A. Kordyuk, S. V. Borisenko, M. Knupfer, and J. Fink. Measuring the gap in angle-resolved photoemission experiments on cuprates. *Physical Review B*, 67:064504, 2003.

[28] A. Kaminski, S. Rosenkranz, H. M. Fretwell, J. Mesot, M. Randeria, J. C. Campuzano, M. R. Norman, Z. Z. Li, H. Raffy, T. Sato, T. Takahashi, and K. Kadowaki. Identifying the background signal in angle-resolved photoemission spectra of high-tempertature cuprate superconductors. *Physical Review B*, 69:212509, 2004.

[29] X. J. Zhou, T. Yoshida, S. A. Keller, P. V. Bogdanov, E. D. Lu, A. Lanzara, M. Nakamura, T. Noda, T. Kakeshita, H. Eisaki, S. Uchida, A. Fujimori,

Z. Hussain, and Z.-X. Shen. Dual nature of the electronic structure of $(La_{2-x-y}Nd_ySr_x)CuO_4$ and $La_{1.85}Sr_{0.15}CuO_4$. *Physical Review Letters*, 86:5578–5581, 2001.

[30] J. L. Tallon and J. W. Loram. The doping depenence of T^* – what is the real high-T_c phase diagram? *Physica C*, 349:53–68, 2001.

[31] Matthias Vojta, Ying Zhang, and Subir Sachdev. Quantum phase transitions in d-wave superconductors. *Physical Review Letters*, 85:4940–4943, 2000.

[32] L. Zhu, P. J. Hirschfeld, and D. J. Scalapino. Elastic forward scattering in the cuprate superconducting state. *Physical Review B*, 70:214503, 2004.

[33] A. Bansil, M. Lindroos, S. Sahrakorpi, and R. S. Markiewicz. Influence of the third dimension of quasi-two-dimensional cuprate superconductors on angle-resolved photoemission spectra. *Physical Review B*, 71:012503, 2005.

[34] R. S. Markiewicz, S. Sahrakorpi, M. Lindroos, Hsin Lin, and A. Bansil. One-band tight-binding model parametrization of the high-T_c cuprates, including the effect of k_z-dispersion. *Unpublished*, cond-mat:0503064v1, 2005.

[35] S. H. Pan, J. P. O'Neal, R. L. Badzey, C. Chamon, H. Ding, J. R. Engelbrecht, Z. Wang, H. Eisaki, S. Uchida, A. K. Gupta, K.-W. Ng, W. E. Hudson, K. M. Lang, and J. C. Davis. Microscopic electric inhomogeneity in the high T_c superconductor $Bi_2Sr_2Ca_1Cu_2O_{8+x}$. *Nature*, 413:282–285, 2001.

[36] John H. Moore, Christopher C. Davis, and Micheal A. Coplan. *Building Scientific Apparatus.* Perseus Books, Cambridge, Massachusetts, 2003.

[37] Robert H. Todd, Dell K. Allen, and Leo Alting. *Manufacturing Processes Reference Guide.* Industrial Press, New York, 1994.

[38] Robert H. Todd, Dell K. Allen, and Leo Alting. *Fundamental Principles of Manufacturing Processes.* Industrial Press, New York, 1994.

[39] Robert L. Powell and William A. Blanpied. *Thermal Conductivity of Metals and Allows at Low Temperatures.* U. S. Government Printing Office, Washington, D. C., 1954.

[40] Robert J. Corruccini and John J. Gniewek. *Thermal Expansion of Technical Solids at Low Temperatures.* U.S. Government Printing Office, Washington, D. C., 1961.

[41] Erik Oberg, Franklin D. Jones, Holbrook L. Horton, and Henry H. Ryffell. *Machinery's Handbook 26^{th} Edition.* Industrial Press, New York, 2000.

[42] A. R. Pelton, J. DiCello, and S. Miyazaki. Optimisation of processing and properties of medical grade nitinol wire. *Minimally Invasive Therapy & Allied Technologies*, 9:107–118, 2000.

[43] Youming Xiao, Heng Sun, Lie Xu, Haidong Feng, and Hongmei Zhu. Thermal contact conductance between solid interfaces under low temperature and vacuum. *Review of Scientific Instruments*, 75:3074–3076, 2004.

[44] Thomas M. Crandell. *CNC Machining and Programming: An Introduction, 2^{nd}.* Industrial Press, New York, 2003.